Chemical Science

ROYAL SOCIETY OF CHEMISTRY

EDGE ARTICLE

View Article Online
View Journal | View Issue

Cite this: *Chem. Sci.*, 2024, **15**, 3339

All publication charges for this article have been paid for by the Royal Society of Chemistry

Received 17th November 2023
Accepted 30th December 2023

DOI: 10.1039/d3sc06165e

rsc.li/chemical-science

NIR-II fluorescence imaging without intended excitation light†

Aiyan Ji,‡[ab] Hongyue Lou,‡[b] Jiafeng Li,[b] Yimeng Hao,[a] Xiaonan Wei,[b] Yibin Wu,[b] Weili Zhao,* [a] Hao Chen*[bce] and Zhen Cheng *[abde]

Nowadays, second near-infrared window (NIR-II) dyes are almost excited by laser diodes, but none of the white light (400–700 nm) excited NIR-II imaging has been studied because of the lack of suitable optical probes. Herein, a novel blue-shifted NIR-II dye, TPA-TQT, has been selected for use in multi-wavelength white light emitting diode (LED) excited NIR-II imaging. This white LED barely caused photo-quenching of the dyes, especially indocyanine green (ICG), whereas the ICG's brightness decreased by 90% under continuous 808 nm laser irradiation. Compared to single-wavelength LED, multi-wavelength LED showed a lower background and similar signal-to-background ratios. This system provided high image resolution to identify blood vessels (103 μm), lymphatic capillaries (129.8 μm), and to monitor hindlimb ischemia-reperfusion and lymphatic inflammation. Furthermore, white LED excited NIR-II fluorescence imaging-guided surgery (FIGS) was successfully performed in 4T1 tumor-bearing mice. Impressively, the lighting LED-based NIR-II FIGS was found to clearly delineate small lesions of metastatic tumors of about ~350 μm diameter and further was able to guide surgical removal. Overall, multi-wavelength LED-based NIR-II imaging is a promising imaging strategy for tumor delineation and other biomedical applications.

Introduction

Second near-infrared window (NIR-II, 1000–1700 nm) fluorescence imaging has been a prominent imaging modality in biomedical fields because of its lower tissue to background ratio, deeper tissue penetration capability and higher signal-to-background ratio (SBR).[1–5] As the cornerstone of fluorescence bioimaging, developing NIR-II fluorophores has been a promising research hotspot for decades. Up to now, diverse NIR-II fluorophores have been developed, including carbon nanotubes,[6] quantum dots,[7] rare-earth nanoparticles[8] and organic fluorescent dyes.[9–12] However, almost all reported NIR-II fluorophores are excited by near-infrared laser diodes, such as 808 nm, 980 nm, and 1064 nm lasers.[13–15] Unfortunately, no NIR-II imaging agents excited by white light (400–700 nm) have been studied. On the one hand, researchers have been committed to developing NIR-II fluorescent dyes with longer emission wavelengths, which will lead to a redshift in the excitation wavelength. All of the these result in a mismatch between the spectra of the NIR-II dyes and the spectral lines of the white light source. On the other hand, to endow dyes with NIR-II imaging capabilities under the excitation of white light, they must have a suitable π conjugation backbone. NIR-II dyes with blue-shifted absorption wavelengths have a better compatibility with the excitation wavelength of white light. Moreover, hypsochromic shift NIR-II dyes exhibit some advantages, such as high fluorescence brightness,[16] and good NIR-II imaging performance.[17] Thus, developing dyes with blue-shifted absorption wavelengths is also a worthwhile attempt for white light-stimulated NIR-II imaging.

Besides developing new fluorescent dyes, another critical issue related to the design of the NIR-II imaging system is the engineering of the excitation light sources for the illumination of the molecular probes. The commonly used excitation light in NIR-II imaging is laser-based light sources, especially 808 nm and 1064 nm lasers, which can penetrate deeper tissues. However, near-infrared lasers can directly reach the retina and cause permanent visual damage.[18] Thus, to avoid eye exposure, researchers need to wear protective goggles. Moreover, high-power lasers can burn tissues and induce photochemical bleaching of the fluorophores.[18,19] In addition, the laser-based

[a]*Department of Pharmacy, School of Pharmacy, Fudan University, Shanghai, 201203, China. E-mail: zhaoweili@fudan.edu.cn*

[b]*State Key Laboratory of Drug Research, Molecular Imaging Center, Shanghai Institute of Materia Medica, Chinese Academy of Sciences, Shanghai, 201203, China. E-mail: haoc@simm.ac.cn; zcheng@simm.ac.cn*

[c]*State Key Laboratory of Chemical Biology, Shanghai Institute of Materia Medica, Chinese Academy of Sciences, Shanghai, 201203, China*

[d]*Shandong Laboratory of Yantai Drug Discovery, Bohai Rim Advanced Research Institute for Drug Discovery, Yantai, Shandong, 264117, China*

[e]*University of Chinese Academy of Sciences, No. 19A Yuquan Road, Beijing 100049, China*

† Electronic supplementary information (ESI) available. See DOI: https://doi.org/10.1039/d3sc06165e

‡ These authors contributed equally to this work.

light sources are relatively expensive. Consequently, a much safer and optimized surgical navigation system is needed. The white light emitting diodes (LEDs), solid-state semiconductor devices, are widely used in commercial and room lighting. In addition, LEDs have been applied to fluorescence microscopic imaging and LED-based phototherapy in the biomedical field.[20–22] Importantly, LEDs are very safe and generate less heat because they emit weak infrared and ultraviolet rays.[23] Finally, low cost, high brightness, and long lifespan make LEDs a promising light source for NIR-II imaging.[20,23] Several studies on NIR-II imaging excited by single wavelength LEDs have been reported.[24–26] Despite all this, previous reports on single wavelength LED-based NIR-II imaging have always focused on the development of fluorophores, with little attention paid to the excitation light sources. Moreover, single wavelength or monochrome LEDs, especially high-energy shortwave blue LED light (415–455 nm), are hazardous to the human retina.[27,28] Comparatively, white LEDs, such as room lighting, flashlights, and other synthetic white LEDs, are widely present in human life. During surgery, the white LED may provide the visual background for the surgical area with good environmental compatibility. However, little effort has been made to explore the use of NIR-II imaging excited by white LEDs.

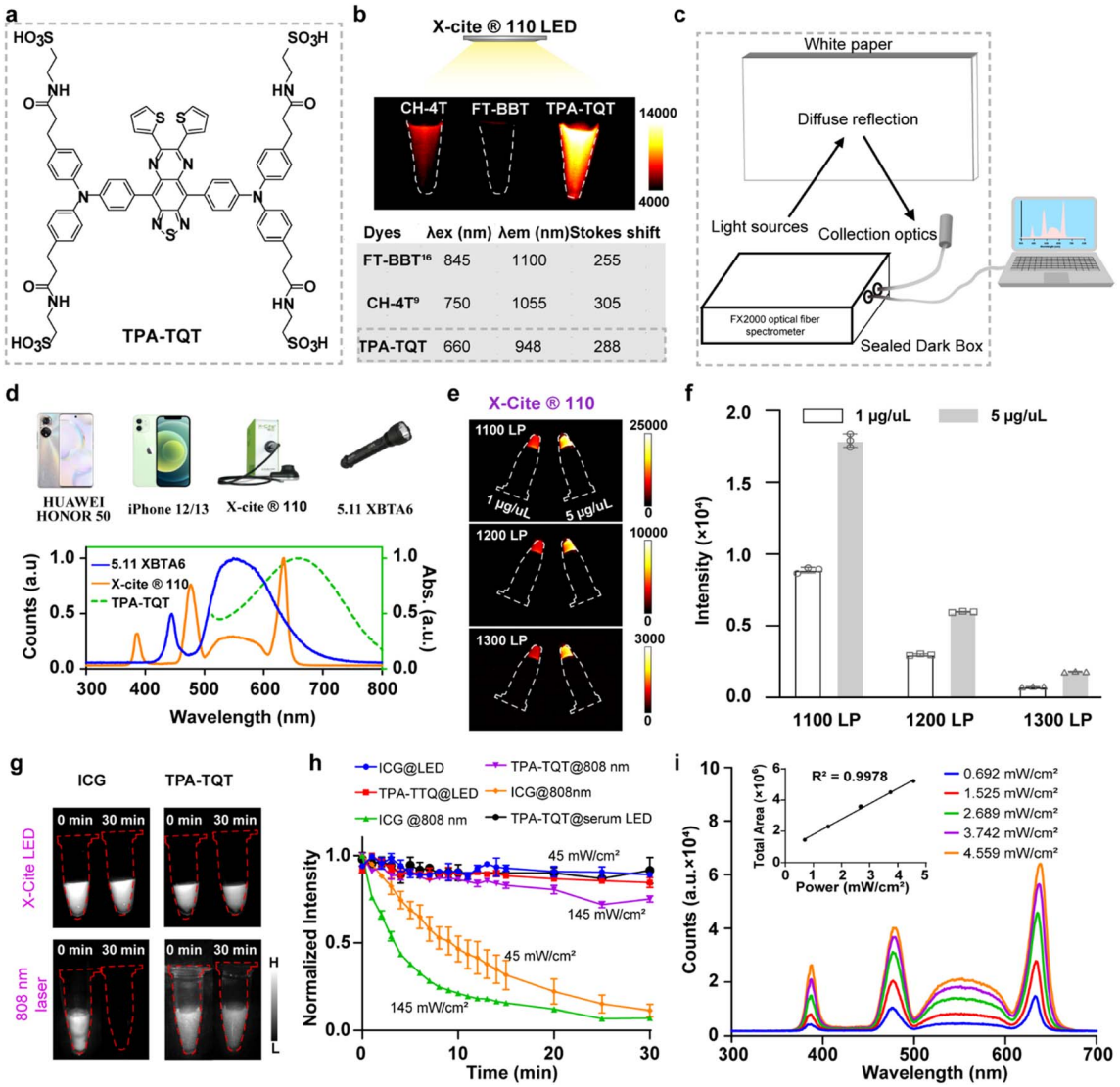

Fig. 1 (a) The chemical structure of TPA-TQT. (b) NIR-II imaging of CH-4T, FT-BBT, and TPA-TQT aqueous solutions at the same concentration (100 μM) under the excitation of X-Cite® 110LED (1000 nm LP, 200 ms, 45 mW cm^{-2}) (top). The optical properties of CH-4T, FT-BBT, and TPA-TQT (bottom). (c) Schematic diagram of the test device for the reflection spectrum of different light sources. (d) Photographs of different LED light sources (top). The absorption spectra of TPA-TQT and the spectral lines emitted by the 5.11 XBTA6 and X-Cite® 110LED (bottom). (e) NIR-II imaging of microcentrifuge tubes containing TPA-TQT aqueous solutions at different long-pass (LP) filters. (f) The fluorescence intensity profiles of TPA-TQT aqueous solutions excited by X-Cite® 110LED in (e). (g) NIR-II imaging of ICG and TPA-TQT under continuous 808 nm laser or X-Cite® 110LED irradiation for 30 minutes. (h) Photostability of ICG and TPA-TQT under continuous 808 nm laser (1000 nm LP, 100 ms, 145 mW cm^{-2} or 45 mW cm^{-2}) or X-Cite® 110LED irradiation (1000 nm LP, 100 or 200 ms, 45 mW cm^{-2}). (i) Spectral lines of X-Cite® 110 light source at different power densities (collection: 300–700 nm). Inset: Plot of the spectral area against the power density of X-Cite® 110LED.

Herein, a novel water-soluble donor–acceptor–donor (D–A–D) NIR-II fluorophore, TPA-TQT (Fig. 1a)[16] has been selected for use with white LED excited NIR-II imaging. Compared to the NIR-II dye we previously reported, TPA-TQT exhibited a blue-shifted absorption maximum. Firstly, the TPA-TQT@BSA-H complex was prepared and displayed an 18.9-fold brighter than that of TPA-TQT. Following that, we evaluated different white LED sources based on *in vitro* NIR-II imaging using TPA-TQT as a fluorophore, including multi-wavelength LED (wavelength range: 360–660 nm, four bands: 385/30 nm, 475/40 nm, 560/80 nm and 640/40 nm) or various broadband LED light sources (410–700 nm). Among them, a multi-wavelength, X-Cite® 110LED-based NIR-II imaging system exhibited good imaging performance and excellent maneuverability. Furthermore, compared to single wavelength LED sources (630/25 nm, 660/25 nm, 730/25 nm LED) and broadband green LED light (450–750 nm), the multi-wavelength LED source, X-cite® 110LED provided a lower tissue background, resulting in superior imaging contrast. This LED-based NIR-II imaging system displayed high resolution and identified blood vessels (103 μm) and lymphatic vessels (129.8 μm) using the TPA-TQT@BSA-H complex as the imaging probe. Moreover, this NIR-II imaging system successfully monitored the process of hindlimb ischemia-reperfusion and imaged the lymphatic inflammation. Further work identified the accuracy and validity of the NIR-II fluorescence imaging-guided surgery (FIGS) excited by multi-wavelength LED. More importantly, broadband LED lighting was able to delineate small lesions of metastatic tumors to aid surgical removal. To the best of our knowledge, this is the first time an LED-excited NIR-II imaging system has been used to remove small lesions of metastatic tumors. This work demonstrates a safer and more effective imaging strategy for scientists and surgeons. It may further facilitate the widespread clinical use of the NIR-II imaging technique.

Results and discussion

The optical/chemical properties of a D–A–D NIR-II dye, TPA-TQT, was first investigated (Fig. 1a and S2a†). The highest occupied molecular orbital (HOMO, −4.83 eV) and the lowest unoccupied molecular orbital (LUMO, −3.06 eV) of TPA-TQT were obtained from DFT calculations with the B3LYP exchange functional employing 6-31G(d) basis sets (Fig. S2b†). The energy gap ΔE of TPA-TQT was 1.77 eV. The maximum absorption wavelength of TPA-TQT was 660 nm (Fig. S2c†). Under the excitation of 655 nm and 808 nm lasers, the TPA-TQT exhibited similar emission patterns, and the emission wavelength covered a range of 800–1300 nm (Fig. S2d†). The chemical stability of ICG and TPA-TQT was measured in the presence of reactive oxygen/nitrogen species (ROS/RNS) (Fig. S2e and f†). The ICG showed a much lower stability after being incubated with ROS/RNS at room temperature for 30 min. However, TPA-TQT was highly resistant to ROS/RNS, and thus, was suitable for accurate *in vivo* imaging. The cytotoxicity of TPA-TQT was also evaluated on the mouse embryonic fibroblast cell line 3T3. After incubation with TPA-TQT for 24 h, no apparent cytotoxicity was observed at a concentration of 100 μM. Meanwhile, the cell viability reached 70% even at high concentrations up to 200 μM, indicating the low cytotoxicity of the TPA-TQT and its high biocompatibility *in vitro* (Fig. S7a†). Furthermore, NIR-II stereo microscopy imaging of TPA-TQT with an 808 nm laser and white LED as excitation light was performed in 4T1 cells (Fig. S7b†). The results showed that TPA-TQT can be used for cellular-level imaging.

During the experiment, TPA-TQT was found to be capable of being excited by white LED room lights with an ultra-low optical density (0.35 mW cm^{-2}) for NIR-II imaging without a laser *in vitro* (Fig. 1a, S1 and S3†). This encouraging result revealed that LED could be used as an excitation light source for NIR-II imaging. However, it was difficult to light up a TPA-TQT aqueous solution with a concentration below 100 μM, under the excitation of LED room light with a long exposure time (1000 ms with a 1000 nm long-pass filter) (Fig. S3†), which prompted us to search for other white LED light sources. Firstly, spectral curves of different LED light sources were measured using an FX2000 fiber spectrometer, including X-Cite® 110LED, mobile phones (iPhone 12, 13, Huawei Honor 50), and a 5.11 XBT A6 flashlight (Fig. 1c, d and S4†). For the X-Cite® 110LED, it displayed four absorption peaks/full width at half maxima (FWHM), 385/30 nm, 475/40 nm, 560/80 nm, and 640/40 nm. Therefore, it was also described as a multi-wavelength LED. Other light sources were all broadband LED light sources, which comprised a high-energy, shortwave blue light band (410–460 nm) and a broadband light at 470–700 nm. Importantly, the emission spectra of these light sources partially overlap with the absorption spectra of TPA-TQT, so they were used as excitation light sources to induce TPA-TQT NIR-II imaging. The TPA-TQT NIR-II imaging was then performed *in vitro* with excitation by different LED light sources (Fig. S5†). Among the tested LED light sources, the 5.11 XBTA6 flashlight and X-Cite® 110LED showed a better imaging performance than other light sources because they have a higher power density. Furthermore, three NIR-II dyes, CH-4T, FT-BBT, and TPA-TQT were selected for X-Cite® 110LED excited NIR-II imaging.[9,16] The results showed that the blue-shifted NIR-II dye, TPA-TQT, exhibited the highest fluorescence brightness, because of a good match between the spectra of TPA-TQT and the spectral lines of the X-Cite® 110LED (Fig. 1b). In addition, the X-Cite® 110LED-induced NIR-II imaging of TPA-TQT solutions *in vitro* was obtained at the 1300 nm sub-NIR-II window (Fig. 1e and f). Moreover, the spectral area of X-Cite® 110LED was proportional to its power density, indicating that the X-Cite® 110LED had a high stability (Fig. 1i). To compare the effects of laser and LED light sources on fluorophores, the photostability of ICG and TPA-TQT were evaluated under the irradiation of these two light sources (Fig. 1g and h). The excellent photostability of TPA-TQT was observed under continuous 808 nm laser irradiation in deionized water for 30 min, and the fluorescence brightness of ICG almost disappeared even at a low power density (45 mW cm^{-2}). Surprisingly, both ICG and TPA-TQT exhibited good photostability when exposed to continuous LED (X-Cite® 110LED) irradiation. Meanwhile, TPA-TQT in serum also exhibited good photostability, which indicated that the LED was a more suitable

excitation light source for NIR-II imaging. Therefore, the X-Cite® 110LED was selected for used as a multi-wavelength LED excitation source in the following experiments.

Previous research used single-wavelength LEDs as the excitation light for NIR-II imaging.[24–26] Thus, the following study compared differences in NIR-II imaging excited by a multi-wavelength white LED and single-wavelength LEDs. Three single-wavelength LEDs (630/25 nm, 660/25 nm, 730/25 nm LEDs) and a green broadband LED light (450–750 nm) were selected as the external excitation lights, and X-Cite® 110LED was used as a multi-wavelength LED (Fig. 2b). Firstly, NIR-II imaging of TPA-TQT aqueous solution with various concentrations excited by different LEDs was evaluated *in vitro* (Fig. 2a and c). Under the same imaging conditions (such as sample concentration, power density, exposure time, and long-pass (LP) filter), *in vitro* NIR-II imaging with single wavelength LEDs and a green LED all displayed higher fluorescence intensity than the multi-wavelength LED: X-Cite® 110LED (Fig. 2d and e). Unexpectedly, the signal-to-background ratio (SBR, the fluorescence intensity of TPA-TQT solution/background) of the X-Cite®

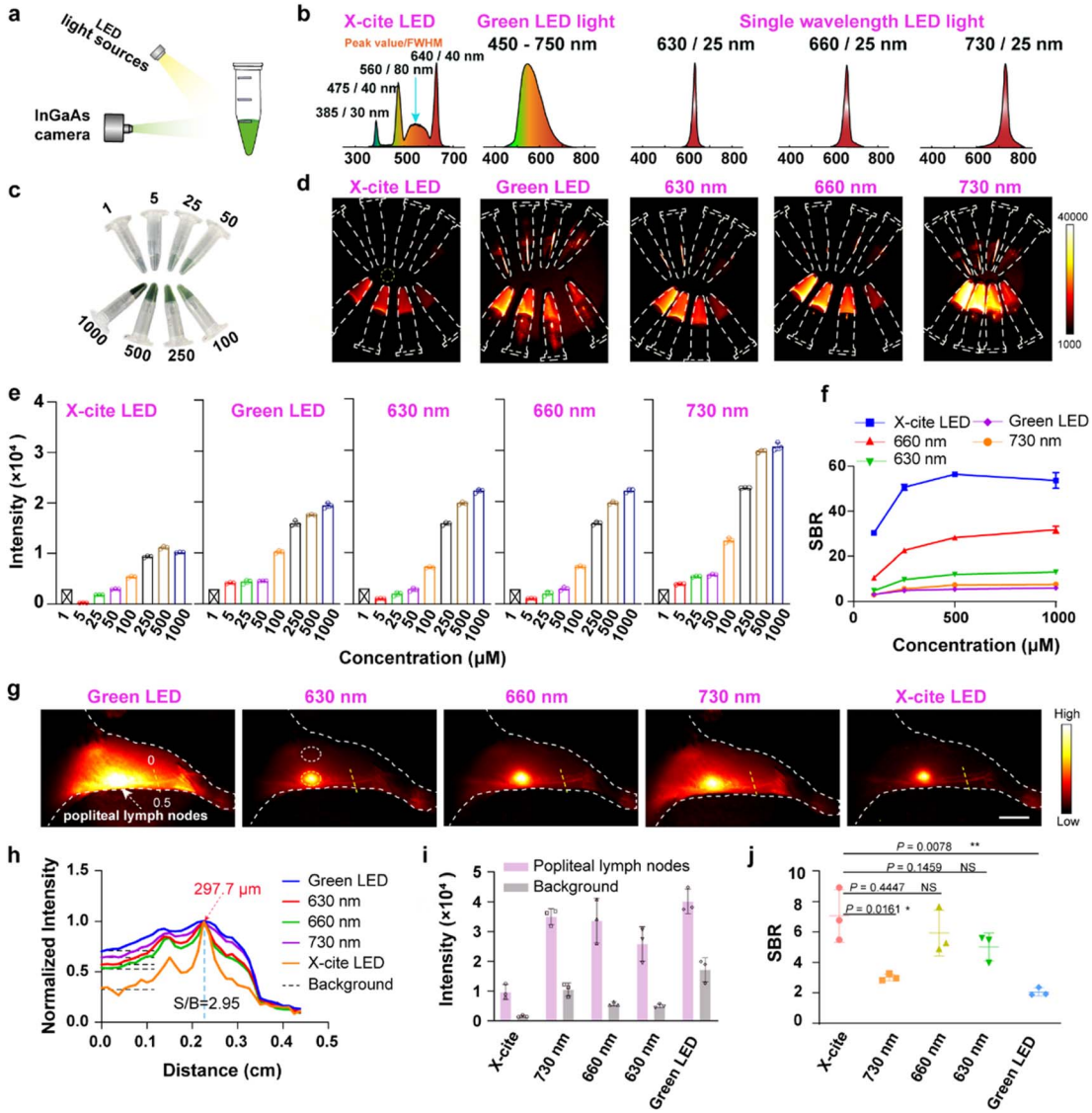

Fig. 2 (a) Schematic of LED light source-based NIR-II imaging system. (b) Schematic illustration of spectral curves of different LED light sources. (c) Photograph of microcentrifuge tubes containing TPA-TQT aqueous solutions of different concentrations (1, 5, 25, 50, 100, 200, 500, 1000 μM). (d) NIR-II imaging of TPA-TQT aqueous solutions under the excitation of different LED light sources in (c) (1000 nm LP, 100 ms, 40 mW cm^{-2}). (e) Fluorescence intensity profiles of TPA-TQT aqueous solutions under the excitation of different LED light sources in (d). (f) The signal-to-background ratio (SBR, defined as fluorescence intensity of different concentrations of TPA-TQT/background (yellow dotted circle) in d) of the NIR-II microcentrifuge tube images as a function of the TPA-TQT concentration. (g) NIR-II lymphatic imaging excited by different LEDs after administration of TPA-TQT (32 μg, 1000 nm LP, 100 ms, 35 mW cm^{-2}), scale bar: 5 mm. (h) The cross-sectional intensity profiles along the yellow dotted lines in (g) with different LEDs as the excitation light. (i) Fluorescence intensity of popliteal lymph nodes (yellow dotted circle) and tissue background (white dotted circle) in (g). (j) The fluorescence intensity ratio of popliteal lymph nodes (yellow dashed circle) and tissue background (white dashed circle) stimulated by different LED light sources in (g). The detailed imaging parameters for each image are listed in Table S1.†

110LED excitation group was significantly higher than that of all the single wavelength LED and green LED groups (Fig. 2f). For example, the SBR of the TPA-TQT solution at 500 μM excited by X-Cite® 110LED reached 56, whereas the SBRs of other groups were much lower than this value. This was because *in vitro* NIR-II imaging excited by X-Cite® 110LED had a lower background than the single wavelength LEDs. Furthermore, the TPA-TQT was injected into the foot pad of a mouse, and a comparison of NIR-II lymphatic imaging stimulated by different LEDs was performed (Fig. 2g). The results showed that the X-Cite® 110LED-based NIR-II imaging was performed with a high resolution and detected the μm-scaled lymphatic vessels with a high SBR (297.7 μm, SBR = 2.95) (Fig. 2h). In contrast, the same region excited by single wavelength LEDs and a green LED displayed blurred vessels and the Gaussian fitting on the lymphatic vessel of the hindlimb failed (Fig. 2h). Although the fluorescence intensity of the popliteal lymph nodes stimulated by X-Cite® 110LED was lower than that of other single wavelength LED and green LED groups, the SBR of the multi-wavelength LED group was higher than those of the green LED and 730 nm single wavelength LED groups, and the SBR was comparable to that of the 630 nm and 660 nm single wavelength LED groups (Fig. 2i and j). The results demonstrated that X-Cite® 110LED was a promising light source for NIR-II imaging.

Encouraged by the above results, the penetration depth of the TPA-TQT was then measured in chicken slices and 1% intralipid under the excitation of X-Cite® 110LED (Fig. 3a, b, S6a and b†). With the increasing penetration depth, the fluorescence intensity of the TPA-TQT gradually decreased, and the capillary profiles gradually blurred. The SBR of the images also decreased with increasing depth (Fig. 3c). The penetration depth of the TPA-TQT *in vivo* was also evaluated, and it could only penetrate 2.5 mm (Fig. S6c†). Furthermore, the feasibility of the NIR-II lymphatic imaging was evaluated using an LED excitation system. In our previous work, dye–protein complexes were found to enhance the dye's fluorescence brightness and provided a superior NIR-II imaging performance.[10,16] Thus, the changes in the fluorescence intensity between TPA-TQT and different proteins (HSA, BSA, and FBS) were evaluated (Fig. S9†). Compared with the TPA-TQT aqueous solution, the fluorescence intensities of TPA-TQT@protein complexes were all enhanced, and this phenomenon was more significant under heating (abbreviated as H). Among them, the fluorescence brightness of TPA-TQT@BSA-H was 18.9-fold and 2.8-fold brighter than TPA-TQT and TPA-TQT@BSA, respectively. The TPA-TQT@BSA-H showed the highest fluorescence brightness and was used in the following experiments. The TPA-TQT@BSA-H and ICG were injected intradermally into footpad of a normal mice. Upon injection, the crowded lymphatic vessels were clearly observed (Fig. 3d, e and S8a†). The lymphatic vessel with a diameter of 129.8 μm was also identified (Fig. 3e). These results showed that the LED excitation system had high potential in NIR-II lymphatic drainage imaging for further clinical translation. The ability of TPA-TQT@BSA-H for *in vivo* lymphatic inflammation detection was further investigated

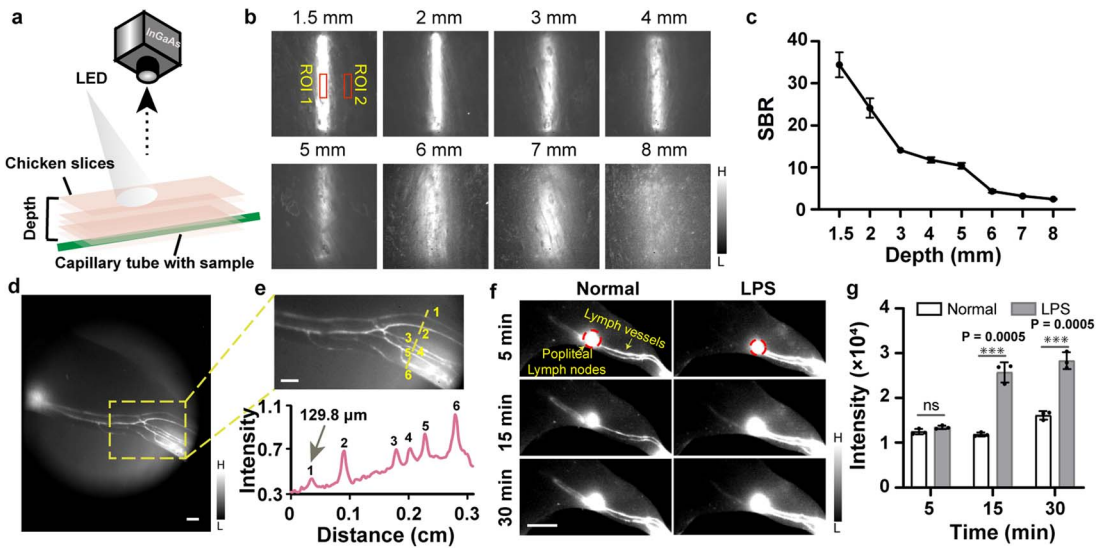

Fig. 3 (a) Schematic illustration of LED-based NIR-II imaging setup for tissue phantom study. (b) NIR-II fluorescence images of capillaries filled with TPA-TQT under chicken slices of different thicknesses (X-Cite® 110LED, 1000 nm LP, 500 ms). (c) Signal-to-background ratio (SBR, defined as ROI 1/ROI 2 in (b) of NIR-II capillary images of the different thicknesses of chicken slices. (d) NIR-II imaging of lymphatic drainage using TPA-TQT@BSA-H complexes as contrast agent (50 μg, X-Cite® 110LED, 1100 nm LP, 200 ms). Scale bar, 1 mm. (e) High-magnification images of the lymph vessels (yellow dotted) in (d) and cross-sectional fluorescence intensity profiles along the yellow dotted lines in (e). Scale bar: 1 mm. (f) NIR-II fluorescence imaging of LPS-treated and normal mouse lymphatic drainage at different times after injection of TPA-TQT@BSA-H (50 μg, X-Cite® 110LED, 1000 nm LP, 500 ms). Scale bar, 5 mm. (g) Fluorescence intensity profiles of popliteal lymph node (red dotted circle in (f)) in LPS-treated and normal groups over time. *P* values were obtained from unpaired two-tailed *t*-tests. The detailed imaging parameters for each image are listed in Table S1.†

using the above LED excitation system. Mice were injected in the footpad intradermally with lipopolysaccharide (LPS) or PBS and 4 h later, this was followed by intradermal or intravenous injection of TPA-TQT@BSA-H for inflammation detection (Fig. 3f). Compared with the control group, the fluorescence intensity of popliteal lymph nodes and the afferent lymphatic vessels in LPS-treated mice increased significantly after 15 min intradermal injection (Fig. 3g). Notably, the efferent lymphatic vessels in LPS-treated mice were barely visible until 15 min after administration of TPA-TQT@BSA-H, while there was no obvious change in the control group as time increased from 5 to 30 min in all the lymph structures (Fig. 3f). Furthermore, LPS-injected paws also showed higher fluorescence intensity than control paws at 16 h after intravenous injection of TPA-TQT@BSA-H (Fig. S8b and c†). These results demonstrated that TPA-TQT@BSA-H NIR-II imaging differentiated between inflammation and normal tissue in living animal models.

To demonstrate the advantages of multi-wavelength LED excited NIR-II imaging, mouse's whole-body vessel imaging ability was compared using different excitation light sources, including a 660 nm/808 nm laser and an X-Cite® 110LED. After administration of TPA-TQT@BSA-H, high-resolution NIR-II vessel imaging was identified under the excitation of X-Cite® 110LED (Fig. 4a). In contrast, 808 nm laser-based NIR-II imaging only distinguished the hindlimb vessels of mice, whereas other abdominal blood vessels were not observed. The 660 nm laser-based NIR-II imaging showed more abdominal blood vessels than the 808 nm laser (Fig. 4a). Significantly, the TPA-TQT@BSA-H NIR-II imaging allowed the observation of dynamic vascular structures within 1 h (Fig. S10†). By comparison, the vessels could only be visualized at 20 s after injection of ICG@BSA-H (Fig. 4a and S10†), which could not offer long-term vascular monitoring using NIR-II imaging technology. Additionally, the abdominal angiography was visualized using sequential long-pass filters from 1000 to 1300 nm under the excitation of the LED (Fig. 4b). Because of the lower tissue absorption, scattering, and autofluorescence at the longer wavelength, the vessels were clearer than those at a shorter wavelength (Fig. 4d). X-Cite® 110LED-excited NIR-II hindlimb imaging was further assessed using TPA-TQT@BSA-H as a contrast agent. High-magnification hindlimb blood vessel networks (Fig. 4c) were discriminated with sequential long-pass filters from 1000 to 1300 nm. The minor diameter of 103 μm among the three parallel hindlimb blood vessels was visualized clearly (Fig. 4e). Collectively, these data indicated that X-Cite® 110LED excited NIR-II imaging gave impressive blood vessel resolution and encouraged us to explore its imaging potential in the following experiments.

Hindlimb ischemia caused by thrombus or atherosclerosis is one of the most common peripheral vascular diseases (PVD).[29]

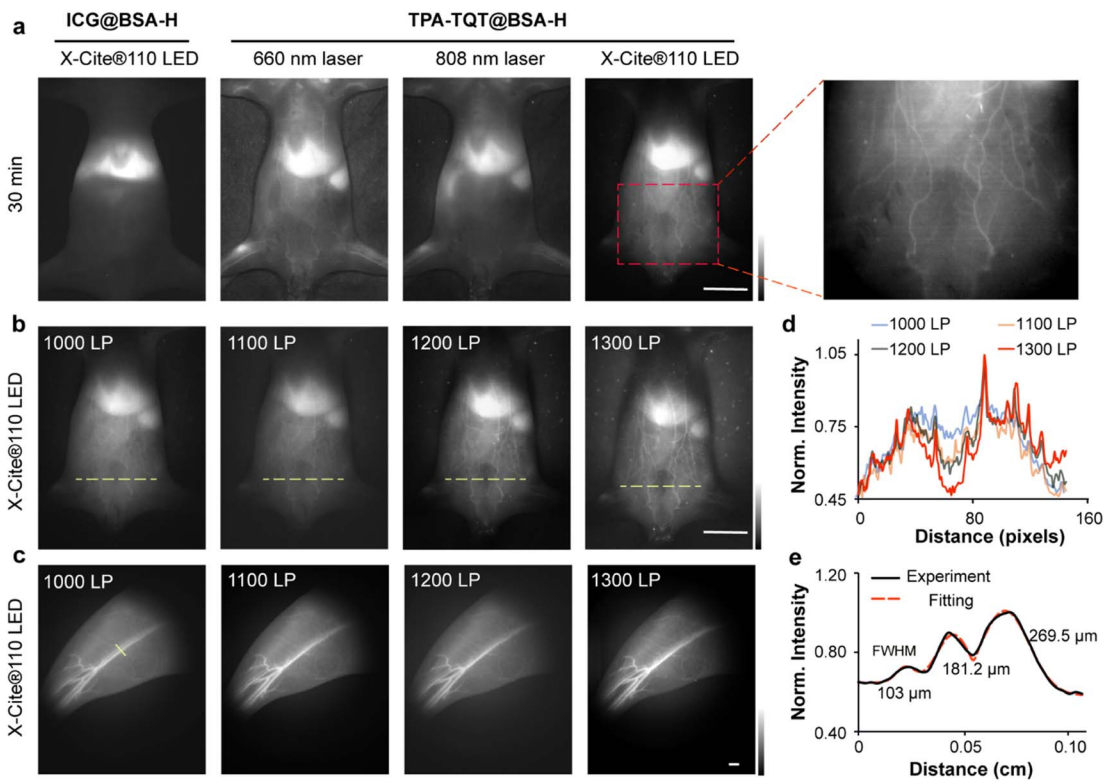

Fig. 4 (a) ICG@BSA-H and TPA-TQT@BSA-H NIR-II imaging excited by different light sources after 30 min administration. Scale bar, 1 cm. (b) The TPA-TQT@BSA-H gives whole-body imaging with different long-pass filters. Scale bar, 1 cm. (c) NIR-II bioimaging of mice hindlimbs at different long-pass filters after TPA-TQT@BSA-H administration. Scale bar, 1 mm. (d) The fluorescence intensity profiles across the yellow dotted lines of interest at different filters in (b). (e) Cross-sectional fluorescence intensity profiles (black solid line) and Gaussian fit (red dotted line) along the yellow line in (c). The detailed imaging parameters for each image are listed in Table S1.†

Functional reconstruction to restore blood flow and real-time observation of the degree of blood reperfusion recovery are of great significance for prognosis evaluation. Here, a murine model of hindlimb ischemia was established by ligating the femoral artery and femoral vein with hemostatic forceps for 30 min to visualize the ischemic reperfusion in limbs (Fig. 5a).[30] The TPA-TQT@BSA-H as the imaging probe, was injected intravenously into the hindlimbs of ischemic mice. The blood flow within the proximal and distal parts of the femoral artery/vein was rapidly visualized by NIR-II window imaging, while removing the hemostatic forceps (Fig. 5b, Movie S1†). In addition, fluorescence intensity profiles of the hindlimb artery and vein at different time points were consistent overall in trends and variability (Fig. 5c and d). Fluorescence intensity was also determined by plotting the cross-sectional intensity profiles along the red dotted line in Fig. 5b of the same vessel imaged in the hindlimb at different time points during 16 s (Fig. 5e). Thus, multi-wavelength LED excited NIR-II imaging provided a feasible strategy for real-time assessment of the process of ischemic-reperfusion.

To demonstrate the feasibility of LED-induced NIR-II imaging for tumor surgery, TPA-TQT-TMS[16] was encapsulated into an amphiphilic DSPE-mPEG2000, to prepare water-soluble and biocompatible NIR-II nanoprobes, TPA-TQT-TMS NPs (Fig. S11a†). The prepared TPA-TQT-TMS NPs were characterized for use in bioimaging applications by transmission electron microscopy (TEM) and dynamic light scattering (DLS) with a hydrodynamic size of 78 nm and a dynamic size of 30 nm (Fig. S11b†). The quantum yield of TPA-TQT-TMS NPs in water was 0.43% with IR-26 (QY: 0.05%) as a reference (Fig. S11d†). The maximum absorption wavelength was 700 nm. The maximum emission wavelength was centered at 948 nm and extended to the NIR-IIa region (1300–1400 nm) (Fig. S11c†). The X-Cite® 110LED-induced NIR-II vascular imaging was first performed on U87MG tumor-bearing nude mice using TPA-TQT-TMS NPs. Immediately after injection, the high-contrast NIR-II imaging of the whole body and tumor blood vessels were clearly distinguished from the surrounding background tissues (Fig. 6b and S12†). Moreover, the vessels at a longer wavelength provided a clearer NIR-II image than those at a shorter wavelength. The above results indicated that superior LED-induced NIR-II vascular imaging avoided unnecessary damage to blood vessels of the surrounding tissue during surgery.

Next, X-Cite® 110LED-induced image-guided tumor surgery was further performed on the 4T1 subcutaneous tumor model (Fig. 6a and S13†). The SBR between the tumor and the surrounding normal tissues gradually increased and peaked at 72 h (the SBR was 6) after TPA-TQT-TMS NPs administration

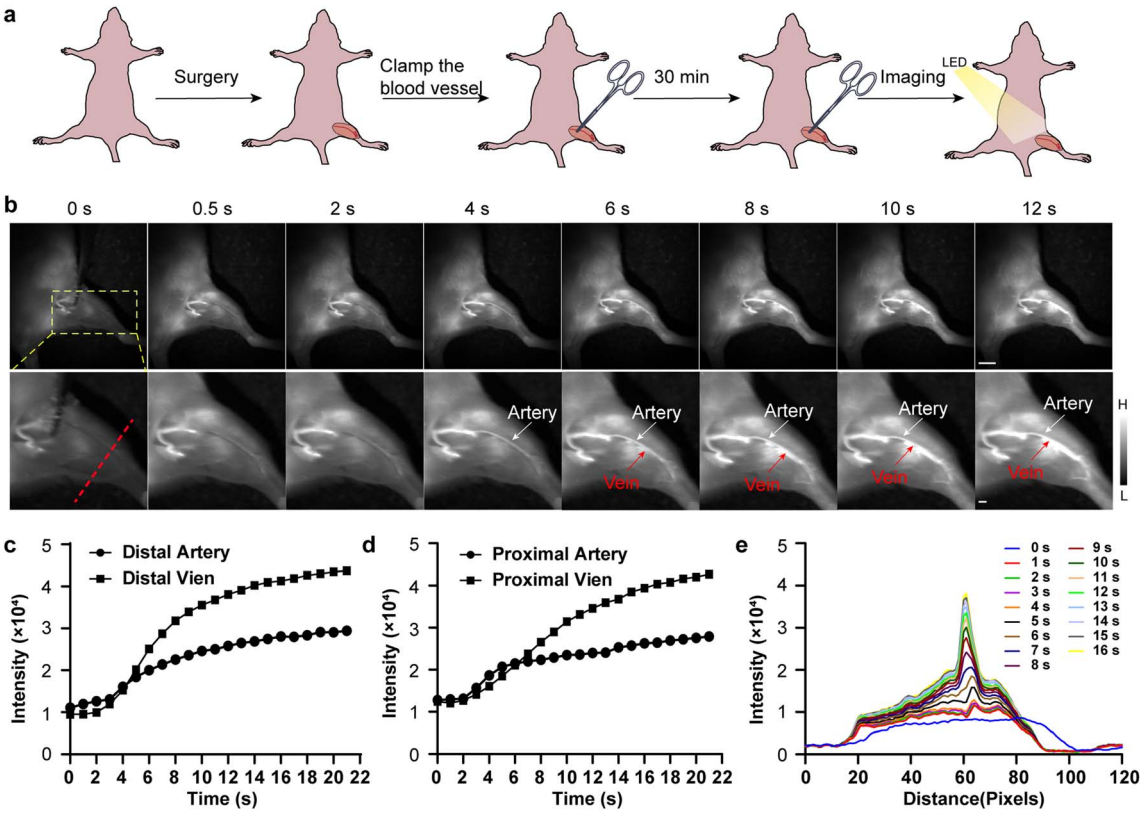

Fig. 5 (a) Schematic illustration showing the hindlimb ischemic reperfusion process. (b) NIR-II imaging of the hindlimb ischemia-reperfusion at different time points after TPA-TQT@BSA-H administration (1000 nm LP, 500 ms, 100 μg). Scale bar, top 5 mm, bottom 1 mm. (c and d) Fluorescence intensity profiles of the hind-limb artery and vein at different time points in (b). (e) The cross-sectional intensity profiles along the red dotted line in (b) at different time points post-injection. Representative images were repeated for $n = 6$ biologically independent mice. The detailed imaging parameters for each image are listed in ESI Table S1.†

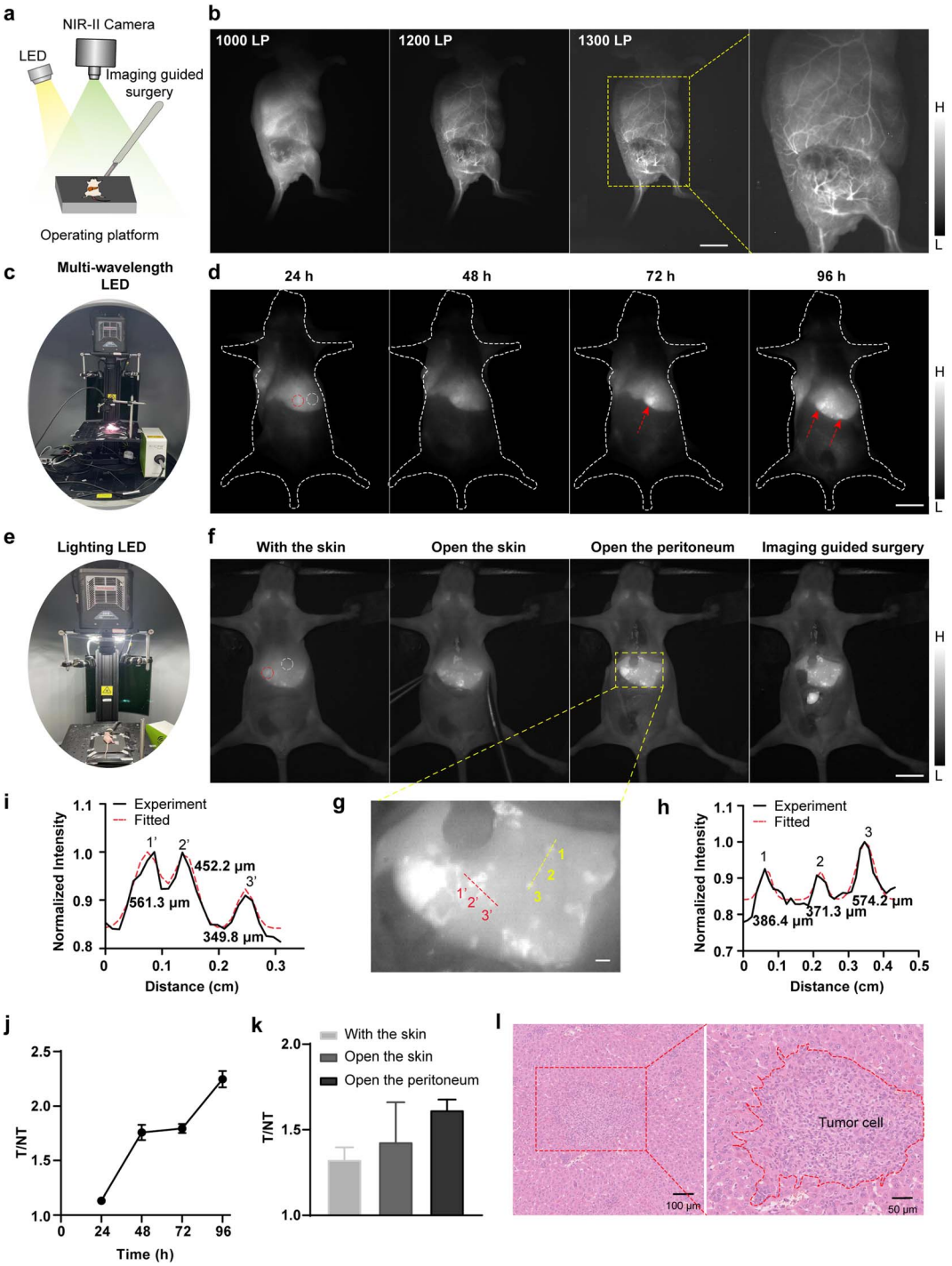

Fig. 6 (a) Schematic illustration of LED-based NIR-II image-guided surgery. (b) NIR-II whole-body vessel imaging of subcutaneous U87MG mouse xenograft model post-injection of TPA-TQT-TMS NPs (366 μg, X-cite® 110LED, 1000 nm LP (300 ms), 1200 nm LP (2000 ms), 1300 nm LP (4000 ms)). Scale bar, 1 cm. (c) Photograph of NIR-II imaging setup excited by multi-wavelength LED (X-cite® 110LED). (d) NIR-II imaging of liver metastasis in 4T1 tumor-bearing mice at different time points after injection of TPA-TQT-TMS NPs (183 μg, X-cite® 110LED, 1000 nm LP, 100 ms). Scale bar, 1 cm. (e) Photograph of NIR-II imaging setup excited by lighting LED. (f) Broadband LED-based NIR-II imaging during fluorescence image-guided surgery at 96 h after TPA-TQT-TMS NPs administration (lighting LED, 183 μg, lighting LED, 1000 nm LP, 1000 ms). Scale bar, 1 cm. (g) The enlarged image of the yellow dotted box in (f). Scale bar, 1 mm. (h and i) Cross-sectional fluorescence intensity profiles (black solid line) and Gaussian fit (red dotted line) along the yellow dotted line (h) and the red dotted line (i) in (g). (j) Tumor (red dotted circle) to normal tissue (white dotted circle) ratios (T/NT) at different time points in (d). (k) Tumor (red dotted circle) to normal tissue (white dotted circle) ratios (T/NT) at different stages of surgical navigation in (f). (l) H&E staining of the 4T1 liver metastatic tumor. The detailed imaging parameters for each image are listed in Table S1.†

(Fig. S13d†). Under these conditions, precise surgical resection of subcutaneous 4T1 tumors was performed at 96 h post injection for mice injected with TPA-TQT-TMS NPs (Fig. S13b, Movie S2†). Surprisingly, multiple liver and intestinal metastases from subcutaneous 4T1 tumors were also clearly observed using LED-excited NIR-II imaging (Fig. 6c and S14†). Under the excitation of X-Cite® 110LED, multiple small lesions of liver metastasis gradually become apparent over time. Unlike subcutaneous 4T1 tumor, the SBR of liver metastasis tumor to adjacent normal liver tissues gradually increased within 96 hours (Fig. 6c, d and j), and this was likely to be because the metabolism of TPA-TQT-TMS NPs in normal liver tissue reduced the background of the normal liver tissues. More surprisingly, LED light used for illumination in the imaging system also excited NIR-II imaging of liver metastases with a considerable imaging contrast and identified μm-scale metastatic lesions (Fig. 6e–i, Movie S3†). Because of the lower tissue absorption and scattering, the SBR of the liver tumors further increased after the skin was cut open (Fig. 6k). Furthermore, all the tumors were further demonstrated by hematoxylin–eosin (H&E) staining (Fig. 6l, S13c and S14b†). Finally, compared to the control group, the H&E staining of the major organs indicated no noticeable pathological change on the subcutaneous 4T1 tumor mice after 4 days of administration of TPA-TQT-TMS NPs (Fig. S15†), except for the presence of tumor metastases in the liver. These results demonstrated that LED-excited NIR-II fluorescence surgical navigation was promising for high-precision and high-efficiency tumor resection.

In this work, the LED-based NIR-II imaging is all performed in the presence of room lighting. It provides excellent visual inspections, which shows that NIR-II imaging is almost unaffected by room lighting.[31] Compared to NIR-I surgical navigation, which requires dimming or turning off room lighting to prevent light interference, the NIR-II imaging system improves surgical efficiency and accuracy.[32]

Nowadays, LED-excited NIR-II imaging is still in its infancy. Our work confirms that this imaging system has a high capability for evaluating vascular/lymphatic structure and function, as well as for surgical navigation. Even μm-scale resolution has been achieved by multi-wavelength LED-excited NIR-II vascular imaging (Fig. 3e and 4c). Meanwhile, this imaging system has also been used to guide tumor resection successfully. It improves the surgical efficiency of tumor resection because LEDs serve as both the excitation and the illumination (Fig. 6). To the best of our knowledge, this is the first time white LED-based NIR-II imaging has been used for image-guided surgery of metastatic tumors. Therefore, this study may accelerate the research on multi-wavelength LED-based NIR-II imaging in biomedicine.

Although the LED excited NIR-II imaging system has been used in various bioimaging scenarios, it only observes surface blood vessels, with a limited imaging field, low power density, and short excitation wavelengths of X-cite® 110LED, which hinders the exploration of deep structural or functional information on animals. In future work, high brightness and long emission wavelength fluorophores should be developed. Meanwhile, active-targeting NIR-II probes need to be developed to improve tumor imaging contrast.[33] Introducing a polyethylene glycol moiety into the optical probes or developing renal-clearable optical agents can improve the uptake of probes in the liver.[34,35] Furthermore, improvements in the imaging equipment, such as equipping it with longer wavelength LED excitation light, are needed to achieve deeper penetration. As one of the primary light sources for clinical endoscopic imaging, the LED-based NIR-II imaging system is expected to be used for various internal examinations of the body in the future, such as colonoscopy and gastroscopy. Additionally, future work will also focus on multispectral NIR-II bioimaging excited by multi-wavelength LEDs to analyze multiple samples simultaneously.

Experimental section

All the experimental details are provided in the ESI.†

Conclusions

In summary, this work reports on a multi-wavelength LED-excited NIR-II imaging strategy for various biomedical applications. With the help of the NIR-II imaging system, high-resolution imaging of tumor vessels, circulatory system, and lymphatic drainage has been achieved with μm-scale resolution. Meanwhile, subcutaneous, hepatic, and intestinal metastatic mouse 4T1 tumors have been successfully identified and resected under LED-based NIR-II imaging guidance. This imaging strategy prepares the way for efficient and precise tumor resection.

Data availability

The data that support the findings of this study are available in the ESI of this article.†

Author contributions

Z. Cheng, H. Chen, W. Zhao, and A. Ji conceived and designed the study. H. Lou, A. Ji, J. Li, X. Wei, and Y. Wu performed *in vivo* and *in vitro* imaging experiments. A. Ji, H. Lou, J. Li, Y. Hao, and H. Chen analyzed the data. A. Ji, and H. Lou drafted the manuscript and which was revised by Y. Hao, H. Chen, and Z. Cheng. All the authors discussed the results and approved the final version of the manuscript.

Conflicts of interest

There are no conflicts to declare.

Acknowledgements

This work was partially supported by the National Natural Science Foundation of China under Grant No. U2267221 (ZC), 82071976 (HC), Shanghai Municipal Science and Technology Major Project (TM202301H003, ZC), the Shandong Laboratory Program (SYS202205, ZC), Science and Technology Innovation

Key R&D Program of Chongqing (CSTB2023TIAD-STX0006, HC), Science and Technology Commission of Shanghai Municipality (YDZX20233100004032001, HC), the National Key Research and Development Program of China (2023YFA1800804, HC), the National Science and Technology Innovation 2030 Major Project of China No. 2021ZD0203900 (HC), and the Lingang Laboratory, Grant No. LG-QS-202206-01 (HC). We are grateful to Gang Liu for his generous help.

Notes and references

1 Y. Liu, Y. Li, S. Koo, Y. Sun, Y. Liu, X. Liu, Y. Pan, Z. Zhang, M. Du, S. Lu, X. Qiao, J. Gao, X. Wang, Z. Deng, X. Meng, Y. Xiao, J. Kim and X. Hong, *Chem. Rev.*, 2021, **122**, 209–268.
2 Z. Lei and F. Zhang, *Angew. Chem., Int. Ed.*, 2021, **60**, 16294–16308.
3 J. Li and K. Pu, *Chem. Soc. Rev.*, 2019, **48**, 38–71.
4 S. He, J. Song, J. Qu and Z. Cheng, *Chem. Soc. Rev.*, 2018, **47**, 4258–4278.
5 G. Hong, A. Antaris and H. Dai, *Nat. Biomed. Eng.*, 2017, **1**, 0010.
6 K. Welsher, S. Sherlock and H. Dai, *Proc. Natl. Acad. Sci. U. S. A.*, 2011, **108**, 8943–8948.
7 H. Yang, R. Li, Y. Zhang, M. Yu, Z. Wang, X. Liu, W. You, D. Tu, Z. Sun, R. Zhang, X. Chen and Q. Wang, *J. Am. Chem. Soc.*, 2021, **143**(6), 2601–2607.
8 X. Zhang, S. He, B. Ding, C. Qu, Q. Zhang, H. Chen, Y. Sun, H. Fang, Y. Long, R. Zhang, X. Lan and Z. Cheng, *Chem. Eng. J.*, 2020, **385**, 123959.
9 A. Antaris, H. Chen, K. Cheng, Y. Sun, G. Hong, C. Qu, S. Diao, Z. Deng, X. Hu, B. Zhang, O. Yaghi, Z. Alamparambil, X. Hong, Z. Cheng and H. Dai, *Nat. Mater.*, 2016, **15**, 235–242.
10 A. Antaris, H. Chen, S. Diao, Z. Ma, Z. Zhang, S. Zhu, J. Wang, A. Lozano, Q. Fan, L. Clew, M. Zhu, K. Cheng, X. Hong, H. Dai and Z. Cheng, *Nat. Commun.*, 2017, **8**, 15269.
11 S. Wang, Y. Fan, D. Li, C. Sun, Z. Lei, L. Lu, T. Wang and F. Zhang, *Nat. Commun.*, 2019, **10**, 1058.
12 Y. Li, Y. Liu, Q. Li, X. Zeng, T. Tian, W. Zhou, Y. Cui, X. Wang, X. Cheng, Q. Ding, X. Wang, J. Wu, H. Deng, Y. Li, X. Meng, Z. Deng, X. Hong and Y. Xiao, *Chem. Sci.*, 2020, **11**, 2621–2626.
13 H. Zhou, X. Zeng, A. Li, W. Zhou, L. Tang, W. Hu, Q. Fan, X. Meng, H. Deng, L. Duan, Y. Li, Z. Deng, X. Hong and Y. Xiao, *Nat. Commun.*, 2020, **11**, 6183.
14 B. Li, L. Lu, M. Zhao, Z. Lei and F. Zhang, *Angew. Chem., Int. Ed.*, 2018, **130**, 7605–7609.
15 M. Wang, D. Yan, M. Wang, Q. Wu, R. Song, Y. Huang, J. Rao, D. Wang, F. Zhou and B. Tang, *Adv. Funct. Mater.*, 2022, **32**, 2205371.
16 A. Ji, H. Lou, C. Qu, W. Lu, Y. Hao, J. Li, Y. Wu, T. Chang, H. Chen and Z. Cheng, *Nat. Commun.*, 2022, **13**, 3815.
17 J. Li, A. Ji, M. Lei, L. Xuan, R. Song, X. Feng, H. Lin and H. Chen, *J. Med. Chem.*, 2023, **66**, 7880–7893.
18 P. Smalley, *Laser Ther.*, 2011, **20**, 95–106.
19 A. Vahrmeijer, M. Hutterman, J. van der Vorst, C. van de Velde and J. Frangioni, *Nat. Rev. Clin. Oncol.*, 2013, **10**, 507–518.
20 P. Oh and H. Jeong, *J. Photochem. Photobiol., B*, 2019, **192**, 1–7.
21 G. Nair and S. Dhoble, *Luminescence*, 2015, **30**, 1167–1175.
22 J. Dong and D. Xiong, *Ann. Biomed. Eng.*, 2017, **45**, 2509–2523.
23 M. Bessho and K. Shimizu, *Electron. Commun. Jpn.*, 2012, **95**, 1–7.
24 F. Wang, L. Qu, F. Ren, A. Baghdasaryan, Y. Jiang, R. Hsu, P. Liang, J. Li, G. Zhu, Z. Ma and H. Dai, *Proc. Natl. Acad. Sci. U. S. A.*, 2022, **119**, e2123111119.
25 X. Fan, Y. Li, Z. Feng, G. Chen, J. Zhou, M. He, L. Wu, S. Li, J. Qian and H. Lin, *Adv. Sci.*, 2021, **8**, 2003972.
26 R. Tian, Q. Zeng, S. Zhu, J. Lau, S. Chandra, R. Ertsey, K. Hettle, T. Teraphongphom, Z. Hu, G. Niu, D. Klesewetter, H. Sun, X. Zhang, A. Antaris, B. Brooks and X. Chen, *Sci. Adv.*, 2019, **5**, eaaw0672.
27 A. Cougnard-Gregoire, B. Merle, T. Aslam, J. Seddon, I. Aknin, C. Klaver, G. Garhöfer, A. Layana, A. Minnella, R. Silva and C. Delcourt, *Ophthalmol Ther.*, 2023, **12**, 755–788.
28 J. Bullough, *J. Illum. Eng. Soc.*, 2000, **29**, 6–14.
29 J. Golledge, *Nat. Rev. Cardiol.*, 2022, **19**, 456–474.
30 B. Li, M. Zhao, L. Feng, C. Dou, S. Ding, G. Zhou, L. Lu, H. Zhang, F. Chen, X. Li, G. Li, S. Zhao, C. Jiang, Y. Wang, D. Zhao, Y. Cheng and F. Zhang, *Nat. Commun.*, 2020, **11**, 3102.
31 Z. Hu, C. Fang, B. Li, Z. Zhang, C. Cao, M. Cai, S. Su, X. Sun, X. Shi, C. Li, T. Zhou, Y. Zhang, C. Chi, P. He, X. Xia, Y. Chen, S. Gambhir, Z. Cheng and J. Tian, *Nat. Biomed. Eng.*, 2020, **4**, 259–271.
32 R. Zhang, A. Schroeder, J. Grudzinski, E. Rosenthal, J. Warram, A. Pinchuk, K. Eliceiri, J. Kuo and J. Weichert, *Nat. Rev. Clin. Oncol.*, 2017, **14**, 347–364.
33 Y. Chen, J. Chen and B. Chang, *iRadiology*, 2023, **1**, 36–60.
34 X. Chen, Y. Hou, M. Tohme, R. Park, V. Khankaldyyan, L. Gonzales-Gomez, J. Bading, W. Laug and P. Conti, *J. Nucl. Med.*, 2004, **45**, 1776–1783.
35 P. Cheng and K. Pu, *Nat. Rev. Mater.*, 2021, **6**, 1095–1113.